This is a repository copy of *Structural study of holmium zirconate nanoparticles obtained through carbon neutral sol-gel process*.

White Rose Research Online URL for this paper:
http://eprints.whiterose.ac.uk/147751/

Version: Accepted Version

Structural Study of Holmium Zirconate Nanoparticles obtained through Carbon Neutral Sol-Gel Process

[1]Suneela Sardar, [1]Girish Kale[*], [1]Mojtaba Ghadiri, [2]Oscar Cespedes

[1]School of Chemical and Process Engineering, University of Leeds. Leeds LS2 9JT, U.K.

[2]School of Physics and Astronomy, University of Leeds. Leeds LS2 9JT, U.K.

*Corresponding Author: g.m.kale@leeds.ac.uk

Abstract:

The pyrochlore oxides are of potential interest as ion conducting electrolyte for intermediate temperature solid oxide fuel cell (SOFC). Nanopowders of holmium zirconate have been synthesised through ion-exchange between sodium alginate gel and metal complex solution followed by its thermal decomposition. Nanoparticles of $Ho_2Zr_2O_7$ were obtained by calcining the dried gel beads at 700˚C for 2h and 6h duration respectively. An insight into calcination has been obtained employing simultaneous thermogravimetric analysis and differential scanning calorimetry (TGA/DSC). Thermal decomposition was also followed using High Temperature X-ray Diffraction (HTXRD) in static ambient atmosphere. Results from TGA/DSC and HTXRD corroborate each other. Fine crystalline nanopowders of single phase $Ho_2Zr_2O_7$ could be obtained after thermal decomposition at relatively low temperature (600-700˚C). Powder X-ray diffraction (XRD) revealed that the material has crystallized as single phase cubic $Ho_2Zr_2O_7$ with defect fluorite structure. XRD and Raman spectroscopy were used to analyse the local structure of holmium zirconate. XRD scans of holmium zirconate and holmium hafnate prepared through identical method have been compared and effect of cationic radius of Zr^{4+} and Hf^{4+} on B-site was studied. The crystallographic data obtained from XRD and transmission electron microscopy (TEM) are in good agreement with each other. This sol gel method referred also as Leeds Alginate Process (LAP) is simple, cost effective, energy efficient and carbon neutral for the preparation of pyrochlore oxides ($A_2B_2O_7$) solid electrolyte material for SOFC.

Keywords: Sodium alginate, Holmium zirconate, Nanoparticles, DSC-TGA, Enthalpy, HT-XRD, TEM-EDX

1. Introduction

Solid Oxide Fuel Cells (SOFCs) are capable of direct utilization of large variety of fuels such as hydrogen, natural gas, coal gas, reformed gasoline and diesel, and gasified carbonaceous

solids (biomass and municipal solid waste) [1-2]. Recently, SOFC technology development effort has focused on improving electrical performance and lowering of the cell operating temperature to 600-800 °C. Formation of greenhouse gases produced in the high temperature combustion process could be eliminated in intermediate temperature solid oxide fuel cells [3].

Pyrochlore materials are used as oxygen electrodes and solid electrolytes in fuel cells [4]. Fundamentally, pyrochlore compounds are characteristic ionic conductors and their functional properties can be changed by varying the processing conditions as well as with the doping of different elements on cation sublattice. Altered materials can also be used in SOFCs as solid electrolytes [5]. An ideal oxide pyrochlore having the formula as $A_2B_2O_7$ can be more accurately written as $A_2B_2O(1)_6O(2)$, where O(1) and O(2) correspond to crystallographically distinct sites of oxygen atoms. Pyrochlore stability can be predicted by tolerance factor which is cations ionic radius ratio (r_A/r_B). For lanthanide pyrochlores the disordered phase forms at equilibrium when $r_A/r_B < 1.46$ [6]. The disordered structure is therefore similar to the mineral fluorite, with a single cation and anion site [7]. Pyrochlores with heavy A-site cations, such as Ho, offer a unique opportunity to study this order/disorder transformation, as disorder can be induced through cation substitution on the B-site.

Sodium alginate is a water soluble polysaccharide extracted from the brown algae. It has varying amounts of α-L-guluronic acid (G) and 1, 4 linked β-D-mannuronic acid (M) residues linked together covalently in different sequence such as -MM-, -GG- structures or -GM- block copolymers. In aqueous solution metal ions interact with alginate [8]. The "zig-zag'' structure of poly-G explains the higher specificity for metal ions as it can accommodate the metal ions more easily [9].

Alginate based synthesis method provide good control over homogeneity and stoichiometry of multicomponent metal oxides nanoparticles [10]. Nanowires of complex metal oxides were synthesised using this method [11]. However, a systematic study to understand thermal decomposition of ion-exchanged alginate to yield complex oxide phases with simultaneous TGA-DSC and temperature programmed XRD has not been reported till todate by any other group of investigators.

This study describes the synthesis of holmium zirconate ($Ho_2Zr_2O_7$) through Leeds Alginate Process (LAP) recently developed and extensively researched by Kale et al [12-14]. Advantage is taken of cheaply available sodium alginate as a promoter for the synthesis of $Ho_2Zr_2O_7$. Nanopowders of holmium zirconate were obtained after thermal decomposition of gelled

precursor. Thermal characterisation of product was carried out using simultaneous thermogravimetric analysis and differential scanning calorimetry (TGA/DSC) and temperature programmed X-ray Diffraction (HT-XRD). Structural and morphological characterisation of the nanoparticles was carried out using X-ray diffraction (XRD), Raman spectroscopy and Transmission Electron Microscopy (TEM) coupled with Energy Dispersive X-ray (EDX) spectroscopy.

2. Materials and Experimental Procedure

Nanopowders of $Ho_2Zr_2O_7$ used to study the structural and morphological properties were obtained using Leeds Alginate Process developed by Kale and co-workers [12-14] is described below.

2.1. Synthesis

Holmium(III) nitrate pentahydrate, $Ho(NO_3)_3*5H_2O$, (purity 99.9%) from Alfa Aesar (Heysham, UK) and Zirconium(IV) oxychloride octahydrate, $ZrOCl_2*8H_2O$, (purity 99.5%) from Sigma-Aldrich (Gillingham , UK) were used to prepare complex metal ions solution. Starting materials were weighed to obtain the molar ratio of $Ho^{3+}/Zr^{4+}=1$ with the concentration of 0.01mol/ml of each cation and dissolved in distilled water using magnetic stirrer. Sodium alginate (Na-ALG) was obtained from Sigma Aldrich Ltd (Birmingham, UK) and a 4 wt% solution was prepared by dissolving an appropriate quantity in distilled water using magnetic stirrer. Both Na-ALG and metal complex solutions were prepared in fume cupboard at ambient temperature and pressure. 200ml of Na-ALG solution was dripped in 200ml of metal complex solution using a burette. The formed beads of gel were allowed to stay in the complex metals solution to facilitate ion-exchange between Na^+ from alginate with Ho^{3+} and Zr^{4+} from aqueous solution under gentle magnetic stirring for 24h. Subsequently, metal-alginate beads were separated from the ionic solution using a stainless steel sieve and extensively rinsed with the distilled water. The metal-alginate beads were eventually dried until constant weight in an oven at 90°C for 24h.

2.2. Characterisation

The dried beads were subjected to thermal analysis using Mettler Toledo STAR^e System (Leicester, UK) for Thermogravimetric Analysis (TGA) and Differential Scanning Calorimetry (DSC) investigations. TGA/DSC analysis was performed from room temperature to 1000°C at the heating rate of 10°Cmin^{-1} under the controlled air environment with steady flow rate of 10mL/min. Mass of dried beads used for TGA/DSC analysis was approximately10mg.

Prior to HT-XRD analysis, a fully dried sample was milled using Retsch Shaker Mill at the frequency of 30Hz using steel ball to obtain fine powder. The milled powder was pressed into an α-Al_2O_3 sample holder for HT-XRD analysis in static ambient atmosphere using CuKα radiation (λ= 1.5418A°) (Anton Paar HTK-1200, Almelo, The Netherlands) at 40kV and 40mA. The temperature program was set from room temperature to 1000°C with the interval of 25°C at the heating rate of 10°Cmin^{-1}. To completely equilibrate the sample at each temperature a dwell time of 30mins was provided. This dwell time was necessary to allow the material to undergo any phase change at specified temperature. HT-XRD scan was performed over the range of 2θ= 20-80° with the step size of 0.03°. Total scan time of 20 min was provided to obtain the information of phase transformation at each temperature. Programmable divergence and antiscatter slits were used for generating constant irradiation length on the sample to improve the data collection statistics at higher angle and reducing the effect of air scattering at low angles which is known to influence the diffraction background patterns. The data was converted from automatic to fixed slit to make it suitable for structural analysis. Resultant data was analysed using X'Pert High Score plus software package supplied by P'Analytical, The Netherland.

Following the conclusions of TGA/DSC and HT-XRD metal-alginate dried beads were calcined at 700°C for 2h and 6h in stationary air. The rate of heating and cooling cycles was maintained at 10°Cmin^{-1} during calcination. After thermal decomposition of dried beads the nanoparticles of $Ho_2Zr_2O_7$ were obtained.

The $Ho_2Zr_2O_7$ obtained after calcination was converted to fine particles using pestle and mortar to break down the agglomerates and analysed using powder X-ray diffraction (XRD Bruker D8) employing CuKα radiation (λ= 1.5418A°) at ambient conditions. A Rietveld size/strain structural refinement was performed on the data obtained from XRD. X'Pert High Score plus software package by P'Analytical was used for Rietveld refinement. Data was comprised of Gaussian and Lorentzian components and a Pseudo-Voigt profile was used to refine the relative proportion of each component during refinement process. Detail of Rietveld procedure can be found elsewhere [15-18].

Raman spectroscopy was used to study the local structure of synthesised nanoparticles of $Ho_2Zr_2O_7$. Raman spectra was collected using a Renishaw Raman system with an excitation laser wavelength of 473nm, 514nm and 633nm, an excitation intensity of 25mW and data acquisition time of 10s. The Raman band of 99% silicon wafer at 520.5±0.5 cm^{-1} was used to calibrate the spectrometer.

Fine powder of holmium zirconate nanocrystal dispersed in acetone was placed on holey copper-carbon grid and analysed using Transmission Electron Microscopy (FEI Tecnai TF20 FEG-TEM, Eindhoven, The Netherlands) to determine the interplananr spacing and morphological features. ImageJ software was used to analyse TEM images. Energy dispersive X-ray (EDX) was used to confirm the elements present and their concentration in order to establish the stoichiometry of the material. Aztec software was used for EDX analysis.

3. Results and Discussion

Metal-alginate dried beads were thermally analysed using simultaneous TGA/DTG/DSC in flowing air and the result are shown in Fig. 1. Thermal decomposition of metal-alginate beads can be divided into seven steps as shown in Table 1. TGA and DSC profile are in good agreement with each other. In the first step, the mass loss is due to the removal of adsorbed water from beads. The twin exothermic peaks were observed in step 2 & 3 which are due to the first stage of partial combustion of organic matrix. More weight loss is involved with the main peak and less with the shouldered end as shown in the inset (a) of Fig. 1. First three steps accompanied with weight loss of 23%. Inset (b) of Fig. 1 shows the data from 150-1000°C to elaborate the DTG curve by reducing its scale. In step 4 and 5 total weight loss is around 25% which is due to the evolution of oxygen resulting from the cleavage of weaker linkage (G-G, G-M, and M-M) in the alginate structure. In steps 4 and 5 onsets of two minor exothermic peaks appears at 247°C and 350°C resulting from the second stage of combustion of organic matrix. The exothermic peak in step 6 is due to the final stage of oxidative decomposition of remainder organic and inorganic matrix resulting into approximately 11% weight loss. Pyrolysis of the organometallic precursor was complete with the endset of major exothermic peak at about 615°C. A small weight loss of about 0.9% can still be observed between 833-900C which may be due to the loss of excess oxygen from the lattice of $Ho_2Zr_2O_{7+\delta}$ that manifests a small endothermic peak in DSC trace. This allows us to estimate an excess oxygen of about ±0.025% in $Ho_2Zr_2O_{7+\delta}$. Based on these results, a calcination temperature of 700°C was selected for further processing of dried alginate beads. These results are in agreement with the $Ho_2Zr_2O_7$ prepared by Polymerized-Complex Method (PCM) [19].

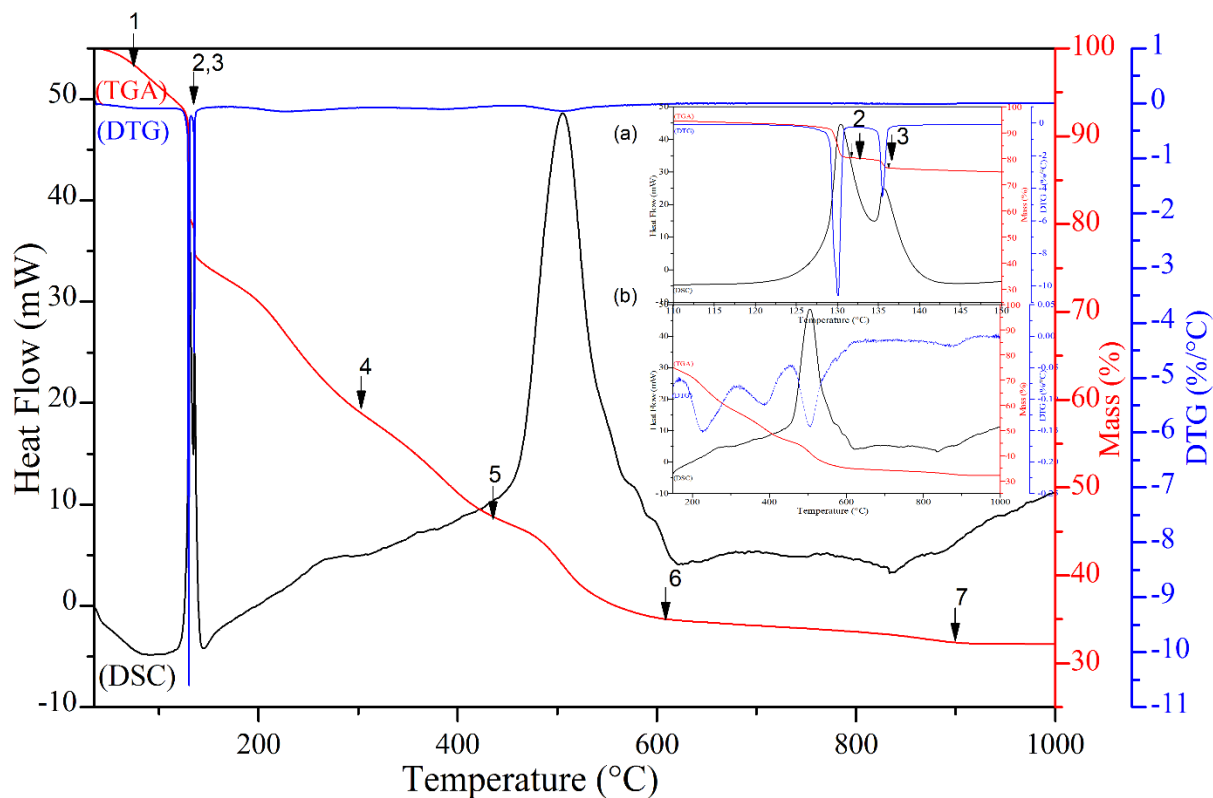**Fig. 1. Thermal analysis of dried beads. Marked arrows show numbered steps.**

Table 1: TGA/DSC analysis

% Weight Loss in TGA curve		
Steps	Temp. Range,˚C	Wt. loss, %
1	RT- 127	7.5
2	127-131	11.9
3	134-137	3.5
4	180-306	14.7
5	327-440	10
6	457-614	10.7
7	833-900	0.9
Peaks in DSC curve		
Peak 1	RT-116 ˚C	Endothermic
Peak 2	116-134˚C	Exothermic
Peak 3	134-145˚C	Exothermic
Peak 4	247-302˚C	Exothermic

Peak 5	350-380˚C	Exothermic
Peak 6	437-616˚C	Exothermic
Peak 7	815-865˚C	Endothermic

Fig. 2 (a) shows the results of HT-XRD patterns of oven dried metal alginate beads from room temperature to 1000°C. No diffraction peaks are observed between 25°C to 300°C as the decomposition of metal-alginate beads has not yet commenced. At 400°C some minor undulation in the baseline were observed at the position close to the diffraction peaks of crystalline $Ho_2Zr_2O_7$. At 600°C, thermal decomposition of beads has completed according to Fig. 1 and high purity single phase holmium zirconate peaks were observed. These results are in excellent agreement with TGA/DSC analysis. A few minor peaks from α-Al_2O_3 sample holder were also noticed along with holmium zirconate peaks as shown in Fig. 2(a).

Fig. 2 (b) shows the refined HT-XRD pattern from 400-1000°C. Here the data is refined to digitally eliminate α-Al_2O_3 sample holder peaks. It is clearly evident that the decomposition started at 400 °C and ended at 600°C yielding a high purity nanoparticles of holmium zirconate. With further increase in temperature from 700-1000°C crystal size increased and sharpness of peaks also increased as a result of crystal growth [12].

Results of thermal decomposition of dried metal alginate beads using TGA/DSC and HT-XRD show high degree of internal consistency with respect to the decomposition temperature of metal alginate beads and also onset and endset of holmium zirconate formation.

Results of TGA/DSC and HT-XRD are in good agreement with each other showing complete thermal decomposition of dried metal alginate beads at 600°C. Based on the results of TGA/DSC/DTG and HT-XRD it can be concluded that the enthalpy change for the decomposition of metal alginate (Ho^{3+}/Zr^{4+}-ALG) into $Ho_2Zr_2O_7$, CO_2 (g) and H_2O (g) is -3826 ± 383 J/g based on the Hess's law of heat summation.

The net enthalpy change of the decomposition process is calculated from the algebraic sum of the area under each peak in the DSC trace divided by the change in weight of the corresponding peak in the TGA trace. The net enthalpy change of -3826 J/g (±10%) suggests that the over all decomposition process is exothermic in nature. It can be envisaged that the evolved heat can be utilized for the drying and calcination process of beads in a continuous manufacturing process or stored if it is produced in excess of the requirements.
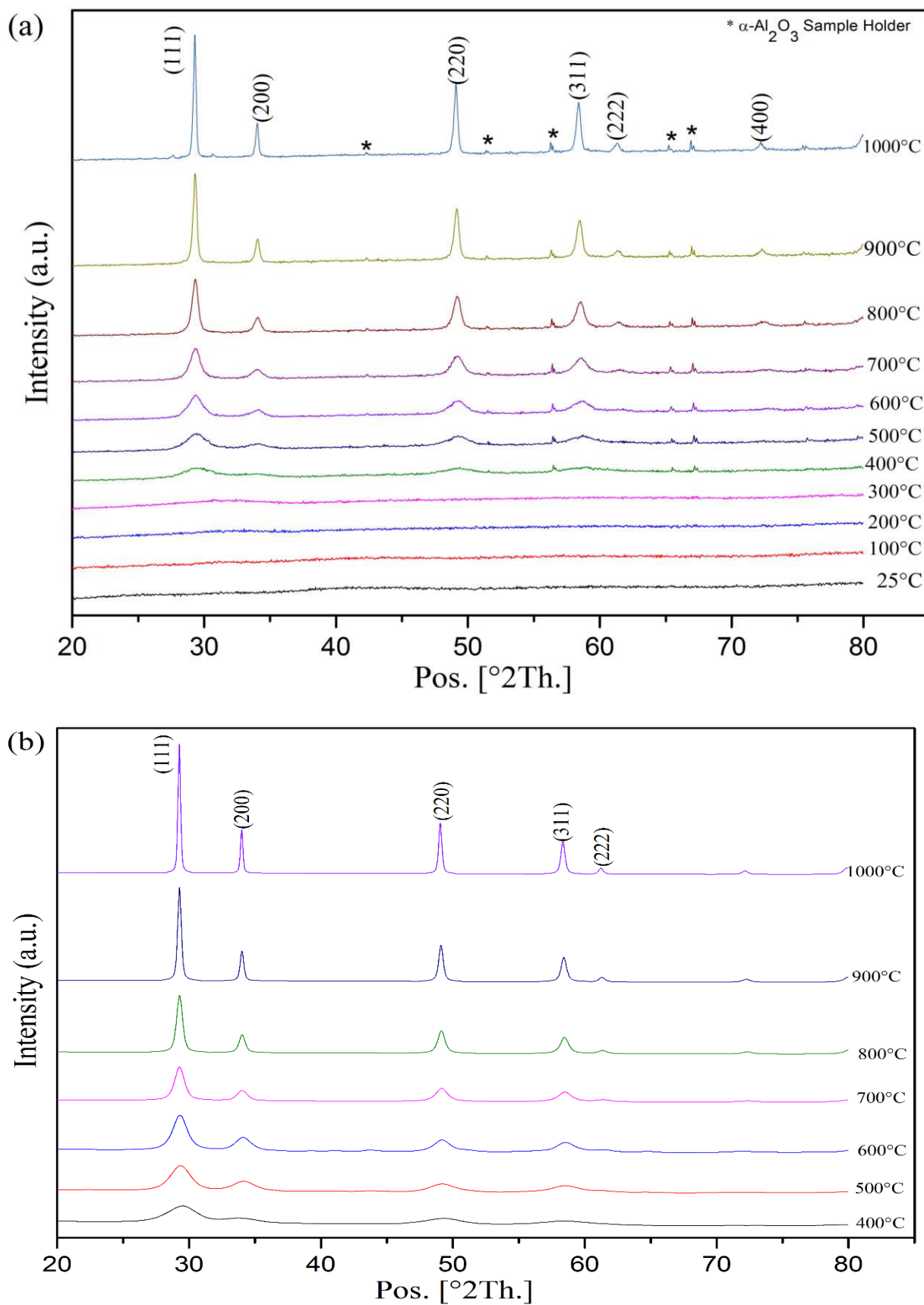
Fig. 2: (a) HT-XRD patterns of dried metal alginate beads from 25-1000°C. The patterns are indexed by ICDD, 01-080-7723 with cubic Ho$_2$Zr$_2$O$_7$ shown at the top of the peaks. Tick marks

'*' for α-Al₂O₃ peaks. (b) Refined HT-XRD patterns from 400-1000°C, sample holder (α-Al₂O₃) peaks were digitally removed.

Fig. 3 shows the XRD pattern of nanopowders obtained after calcination of dried beads at 700°C for 2h and 6h. The observed data for different calcination durations yielded single phase $Ho_2Zr_2O_7$ having cubic defect fluorite structure. XRD pattern of material calcined for 2h shows broader peaks compared with that of 6h. Broadening of peak is one of the indicator of presence of nano-sized crystallites.

Effect of calcination duration on crystallite size is shown in Table 2. Crystallite size increased with the increase in annealing time. This phenomenon is known as Ostwald ripening in which inhomogeneous structure changes over time and larger crystals are formed at the expense of small ones to yield relatively more stable structure [20] also commonly observed during the powder sintering processes.
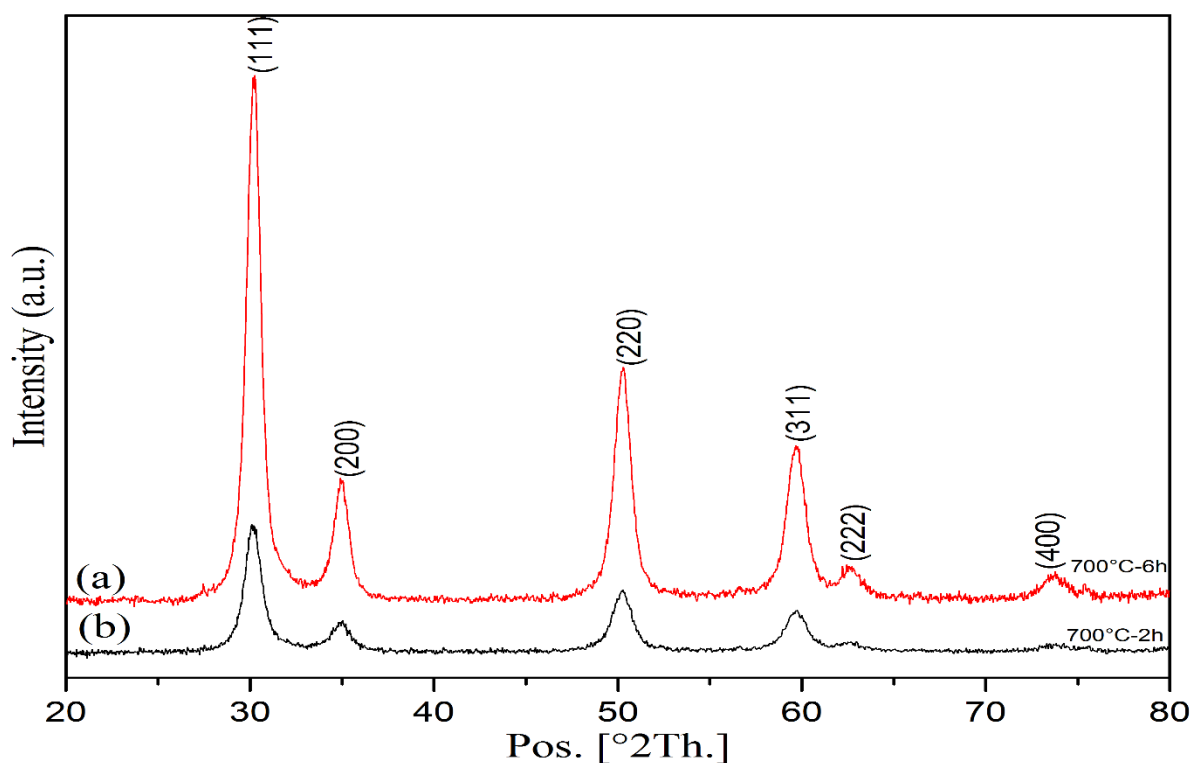

Fig. 3: XRD patterns of Ho₂Zr₂O₇ nanoparticles obtained after calcination at 700°C for (a) 2h and (b) 6h. Patterns are indexed by ICDD, 01-080-7723 at the top of the peaks.

The Rietveld refinement of XRD pattern of holmium zirconate (Ho₂Zr₂O₇) calcined at 700˚C for 6h is shown in Fig. 4. The observed and calculated patterns matched with each other and peaks could also be indexed with the XRD reference pattern (ICDD, 01-080-7723). The value of goodness of fit (GOF) is close to 5% as seen in Table 2.

Crystallite size was obtained from XRD pattern using Scherrer equation after eliminating instrument broadening and stress-strain broadening. The original data and refined model are in excellent agreement with each other and the value of weighted residual (Rwp) from refinement is 7%. With the increase in annealing time from 2h to 6h, particle coarsening occurred and correspondingly micro-strain decreased as anticipated. Coarsening resulted in crystal growth from approximately 6nm to 8nm. The unit cell parameters of the nanopowder of $Ho_2Zr_2O_7$ having defect fluorite structure (a = b = c = 5.148 A° and α = β = Γ = 90°) prepared through ion-exchange based sol-gel method in this study is in excellent agreement with the data obtained through Polymerized-Complex Method (PCM) [19] and gel combustion technique followed by high temperature sintering [21].
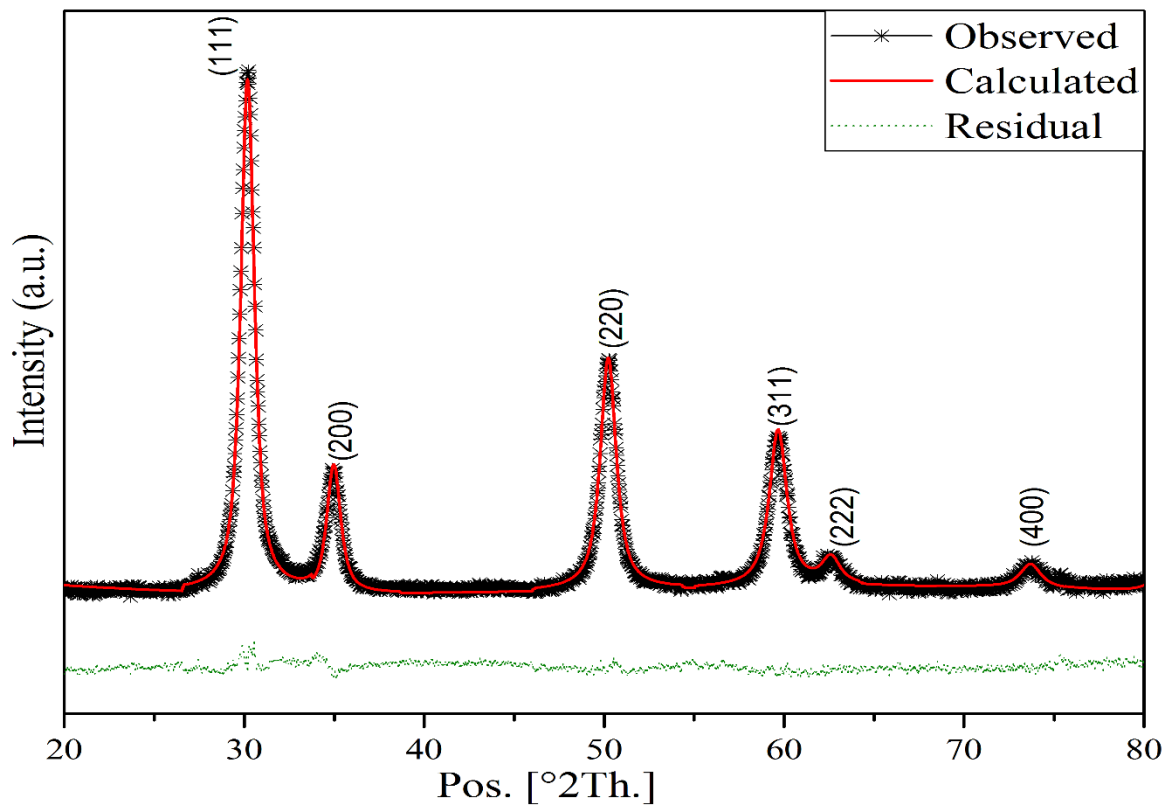

Fig. 4: Rietveld refinement of XRD patterns of $Ho_2Zr_2O_7$ nanoparticles obtained after calcination at 700 °C for 6h. Miller indices representing fluorite structure are shown on the top of the peaks.

Table 2: Structural properties of $Ho_2Zr_2O_7$

Sample	Rietveld Refined Size Strain Analysis					
	Avg. Crystallite Size (nm)	Micro Strain (%)	R_{wp} (%)	R_{exp} (%)	GOF $=(R_{wp})^2/(R_{exp})^2$	Lattice Parameters (A°)
700°C-2h	6.27	2.478	5.843	5.276	1.226	5.149734

| 700°C-6h | 7.85 | 2.042 | 6.971 | 3.037 | 5.266 | 5.147994 |

Fig. 5 shows the comparison between the XRD patterns of holmium hafnate ($Ho_2Hf_2O_7$) [22] and holmium zirconate ($Ho_2Zr_2O_7$) synthesised through alginate based sol gel method. In many aspects Hf is considered chemically identical to Zr, since they belong to the same group of the periodic table. Hf^{+4} and Zr^{+4} have ionic radii of 0.71A° and 0.72A° for six fold coordination respectively [23]. Cation with larger ionic radius (Zr^{+4}) shows that the fluorite peaks have shifted slightly to the lower angle as seen in the insets of Fig. 5 which is in agreement with the larger unit cell parameter of $Ho_2Zr_2O_7$ compared with $Ho_2Hf_2O_7$ [22] by approximately 5%.
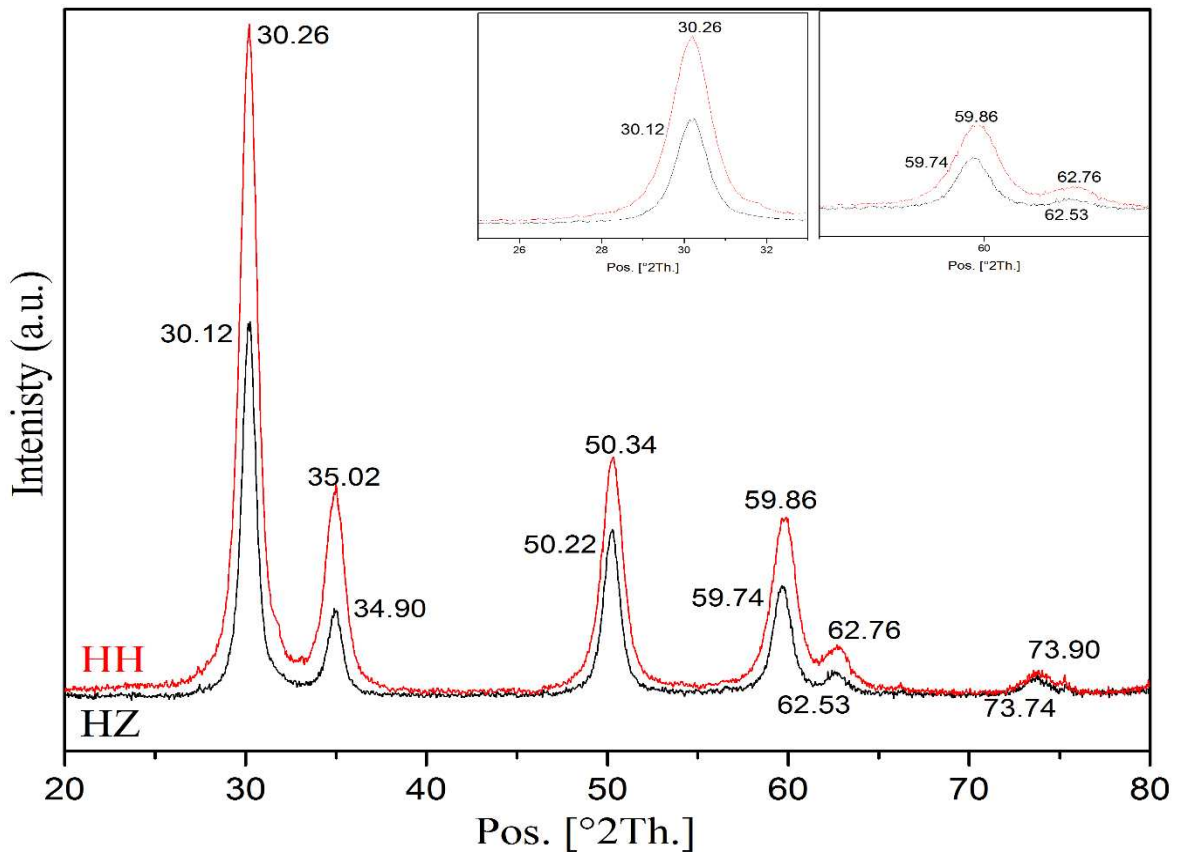

Fig. 5: XRD patterns of homium hafnate (HH) and holmium zirconate (HZ) synthesised through alginate method. Insets show the shifting of peak positions.

XRD technique is more restrained to disorder in cation sub-lattice rather than in anion sub-lattice since the scattering power of X-rays for oxygen is much lower than rare-earth and transition metal cations. On the other hand, Raman spectroscopy is sensitive to metal-oxygen vibrations compared with metal-metal vibrations in oxides. Hence, Raman spectroscopy is an excellent technique to analyse the extent of disorder in pyrochlore oxides and differentiate between the pyrochlore and defect fluorite structures [24]. Factor group analysis predicted that there are a total of six Raman active modes in pyrochlore oxides [25].

11

$$\Gamma_{Raman} = A_{1g} + E_g + 4F_{2g} \qquad (1)$$

Raman spectra of $Ho_2Zr_2O_7$ nanopowder obtained after calcination at 700˚C for 6h is shown in Fig. 6. Individual modes are indistinguishable in fully disordered defect-fluorite [26-28] structure, the spectra here shows some initial pyrochlore type short range ordering of cation and oxygen vacancies [26-28] and appearance of weak bands is due to partial ordering of fluorite structure [21]. Bands around 270 and 590cm^{-1} correspond to the Zr−O vibrations. The band at 590 cm^{-1} is assigned to F_{2g} mode due to Zr−O stretch [21]. Bands around 665 and 883cm^{-1} correspond to the Ho−O vibrations. The vibrations corresponding to Ho−O and Zr−O appear in band 1060 cm^{-1}. Band around 491cm^{-1} clearly indicates the presence of disordered defect fluorite structure. The transformation from ordered pyrochlore structure to disordered defect fluorite structure shows the broad hump around 350-400 cm^{-1} [21] is not noticed since the compound is single phase fluorite. A band around 531cm^{-1} is also absent here which is strictly assigned to the A_{1g} mode of pyrochlore phase [29].
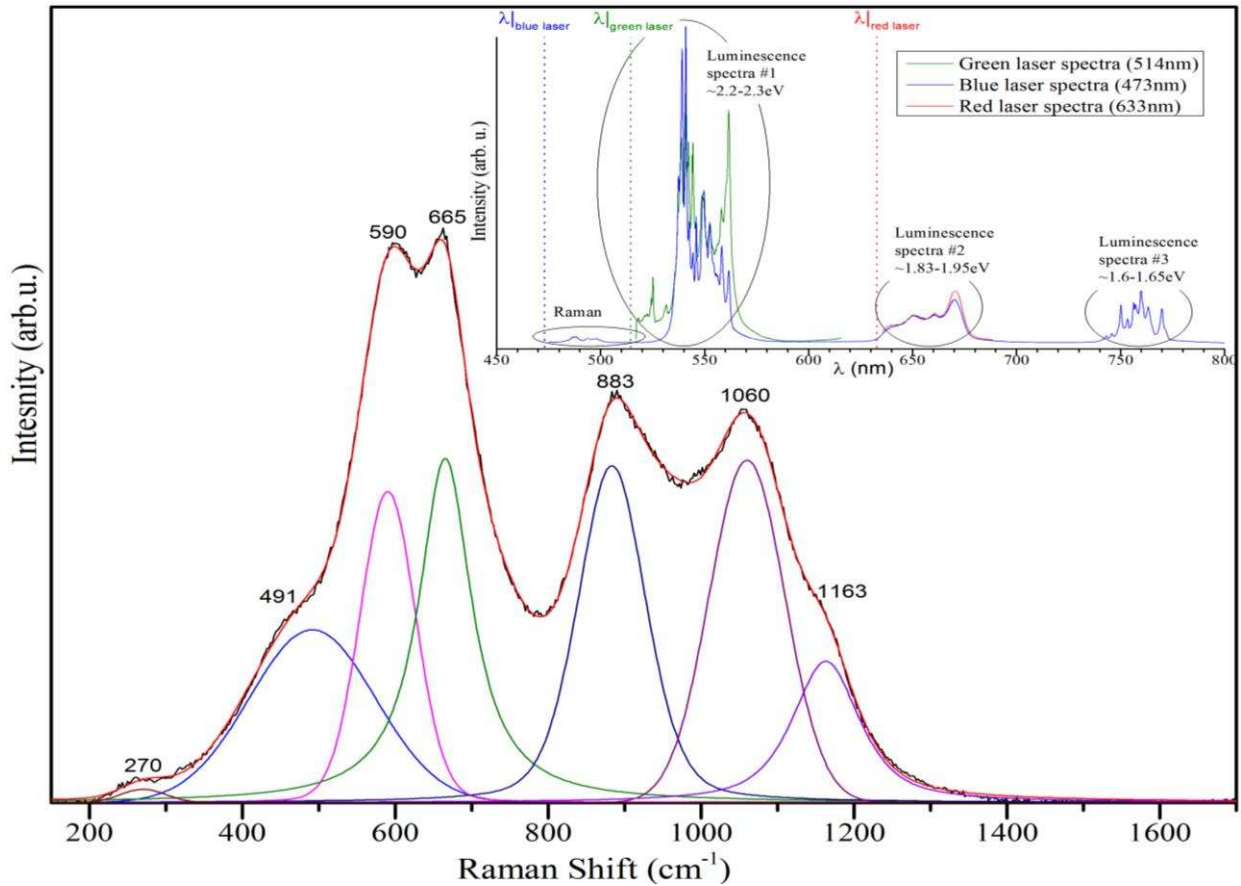

Fig. 6: Raman spectra of $Ho_2Zr_2O_7$ nanopowder obtained after calcination at 700˚C for 6h. Spectrum with laser wavelength of 473nm along with peaks fitting. Black curve is original Raman spectrum and red is fitted one. Inset shows the luminescence spectra for three different lasers blue-473nm, green-514nm and red-633nm.

Inset in Fig. 6 shows the luminescence spectra of $Ho_2Zr_2O_7$ nanopowders at different wavelengths. First luminescence spectra with excitation wavelength of 514nm appeared at the range of 520 to 560nm. Second luminescence spectra using excitation wavelength of 633nm appeared at wavelength from 635 to 680nm. Third one with 473nm blue laser was observed from 740 to 770nm.

TEM images and SAED pattern of $Ho_2Zr_2O_7$ nanopowder obtained after calcining at 700˚C for 6h are shown in Fig. 7. Holmium zirconate nanoparticles were of uniform shape with narrow size distribution and crystalline in nature. The interplanar spacing of nanocrystalline $Ho_2Zr_2O_7$ were calculated from the SAED pattern and were assigned unique Miller indices. The Miller indices (hkl) of all the crystal planes of $Ho_2Zr_2O_7$ obtained from SAED pattern are in good agreement with XRD reference pattern (ICDD, 01-080-7723) and the XRD pattern shown in Fig. 3 & 4. Table 3 shows the d-spacing calculated from TEM and XRD data for different planes. Interplanar spacing (d-spacing) calculated from the XRD and TEM (SAED) are in excellent agreement with each other and reference pattern as shown in Table 3.

TEM is one of the few techniques that allows real space visualisation of nanoparticles [30] Average particle size of $Ho_2Zr_2O_7$ obtained from TEM image analysis is 9±1nm and average crystallite size from XRD is 8nm (Table 2). The particle size determined by TEM analysis and the crystallite size calculated from refinement of XRD data are in excellent agreement with each other in spite of the fact that the particle dimensions obtained from these two complimentary analytical techniques corresponds to the dissimilar orientation of the nanopowders [31].

Table 3: Comparison of d-spacing of Holmium Zirconate from TEM, XRD Rietveld refinement and XRD reference pattern

h	k	l	Ref. (ICDD, 01-080-7723) d, A˚	XRD d, A˚ 700˚C-6h	TEM d, A˚ 700˚C-6h
1	1	1	3.01450	2.959	3.01
2	0	0	2.61060	2.566	2.61
2	2	2	1.84600	1.819	1.82
3	1	1	1.57430	1.550	1.55

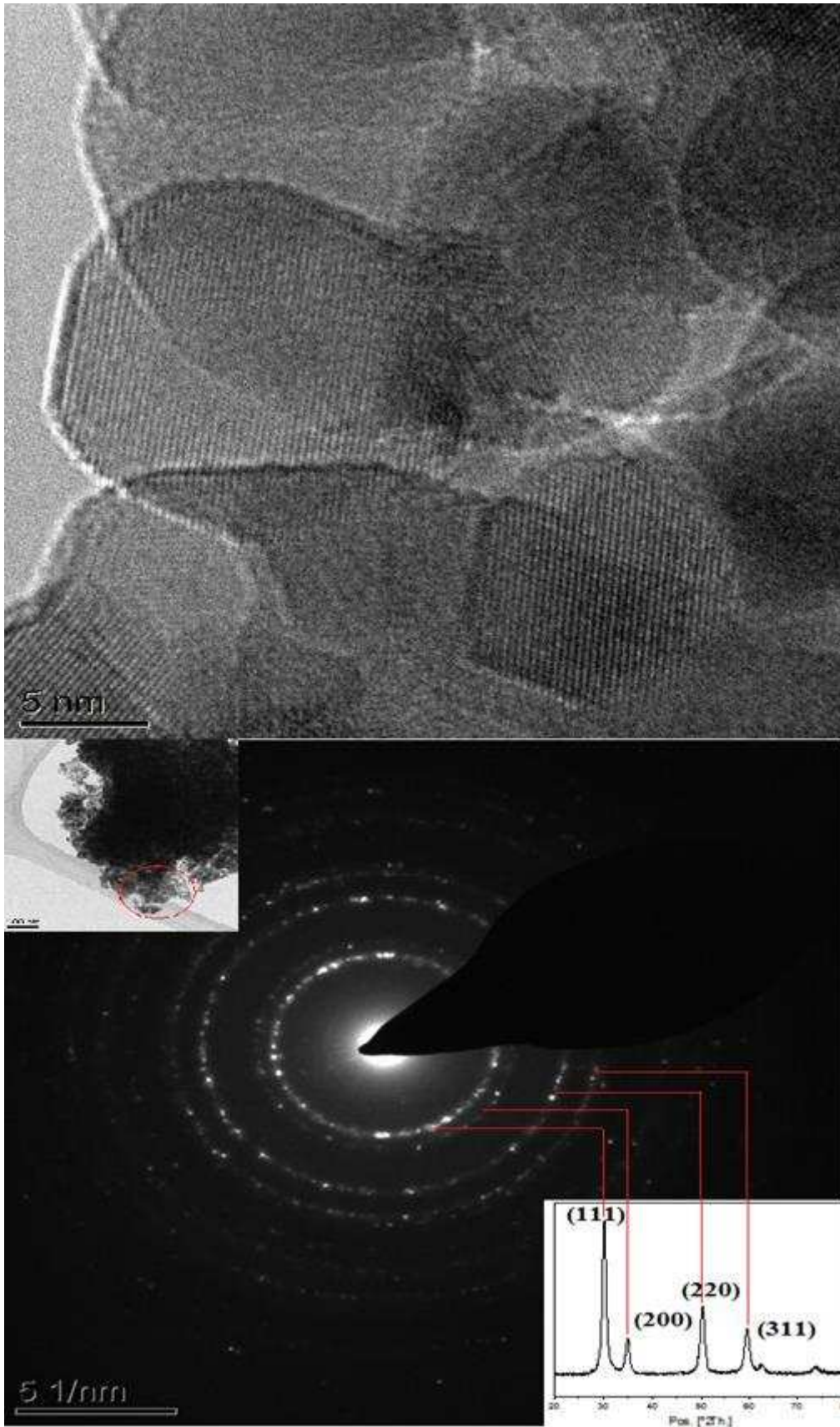**Fig. 7: TEM images with SAED pattern of Ho₂Zr₂O₇ calcined at 700˚C for 6h. SAED pattern indexed with XRD peaks**

Fig. 8 shows the TEM-EDX spectrum of nanopowder of holmium zirconate. To further confirm the composition of the synthesised material EDX analysis was performed. $Ho_2Zr_2O_7$ nanocrystals are composed of holmium, zirconium and oxygen with an atomic ratio of 2 : 2 : 7. The peaks due to Cu and C in the spectrum are attributed to the holey carbon mesh grid used for TEM analysis. The Inset in Fig. 8 shows the atomic % of elements obtained from EDX and stoichiometry with error bars. This agrees well with the theoretical values of 18.2% for Ho, 18.2% for Zr and 63.6% for O indicating that compound exhibit negligible non-stoichiometry. The percentage error in the elemental analysis is less than 0.2%.
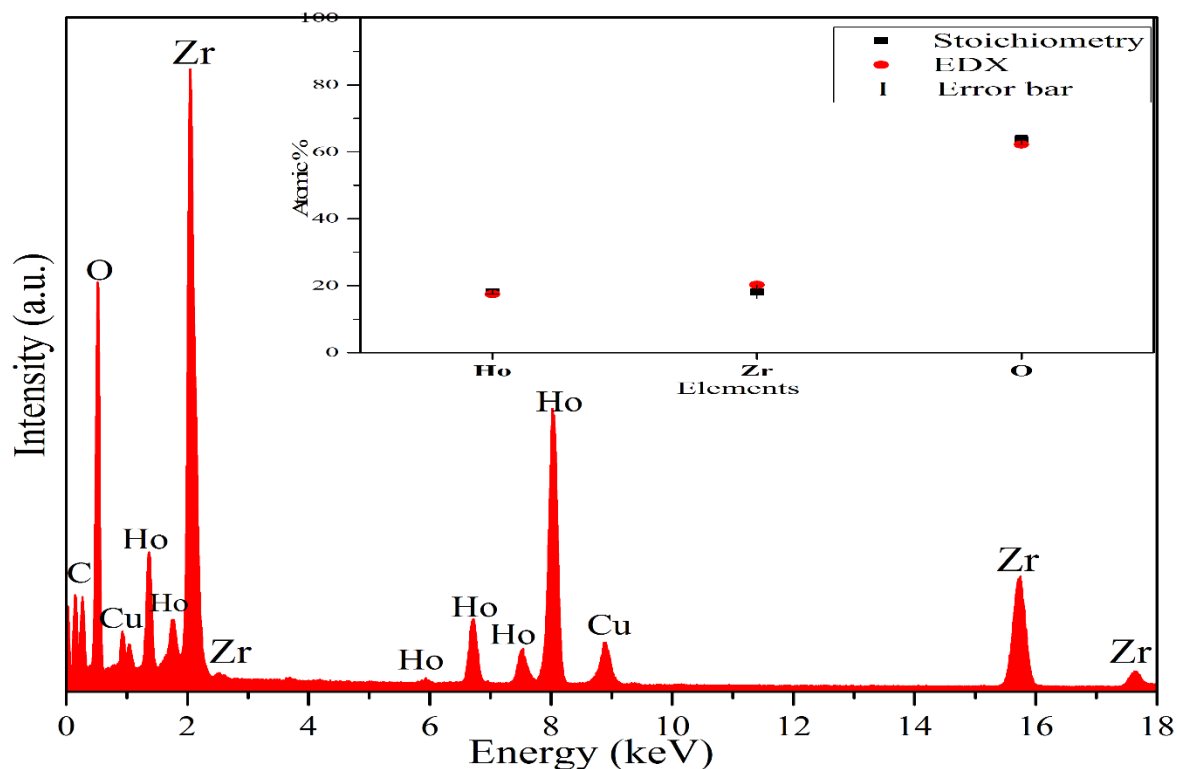

Fig. 8: TEM-EDX spectrum of $Ho_2Zr_2O_7$ calcined at 700˚C for 6h. Inset compares the atomic % of elements with the stoichiometry.

Fig. 9 shows the surface profile imaging of $Ho_2Zr_2O_7$ nanopowder calcined at 700˚C for 6h using High Resolution TEM (HRTEM) which is capable of showing the unidirectional images of the top surface layer, i.e. a profile view [32]. The main advantage of HRTEM is to allow examination of crystal phases in an overlapping nanopowder sample [33].

Lattice planes can be easily seen and indexed as (111) and (222) in Fig. 9. Nanoparticles of $Ho_2Zr_2O_7$ showed the crystalline phase formation with cubic structure and interplanar distance of 3.0 A˚ and 1.82 A˚ for (111) and (222) planes, respectively. Using high purity feed material nanoparticles of $Ho_2Zr_2O_7$ can be successfully prepared using Leeds Alginate Process (LAP).
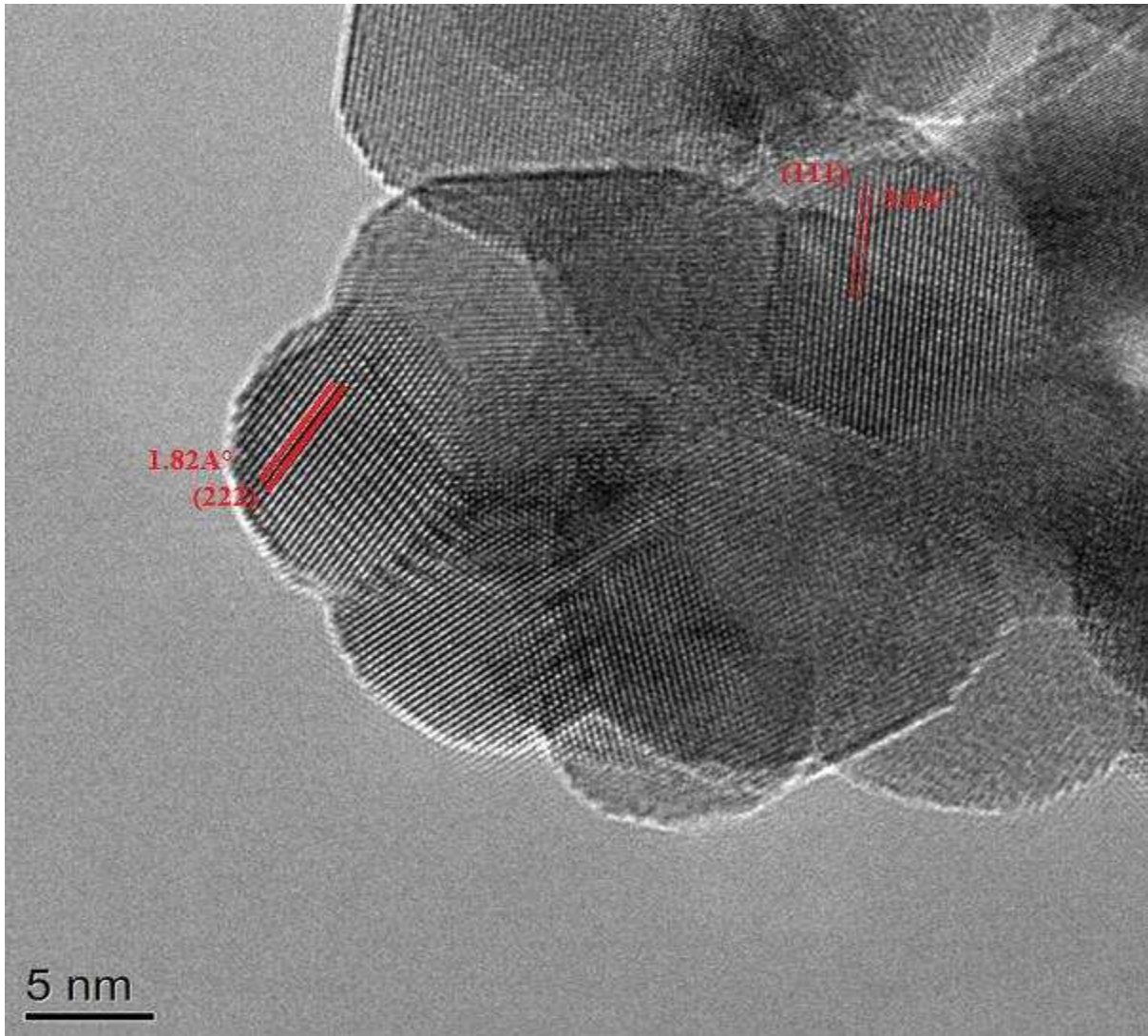
Fig. 9: HR-TEM image of Ho₂Zr₂O₇ nanopowder with defect fluorite structure and interplanar spacing of 3.0 A° and 1.82 A° along the (111) and (222) planes respectively.

4. Conclusions

An alginate based sol-gel technique was employed to prepare nanoparticles of holmium zirconate at 600 ˚C. Beads of precursor were obtained by carrying out ion-exchange between complex metal-ion solution and sodium alginate gel. Nanopowder of holmium zirconate were successfully obtained after calcination of precursor beads. TGA/DSC and HT-XRD analyses yield decomposition temperatures that are in good agreement with each other and an optimum calcination temperature of 700˚C was determined. XRD analysis confirmed that single phase cubic nanoparticles of Ho₂Zr₂O₇ with defect fluorite structure and space group of Fm3̄m were successfully prepared. Analysis from Raman spectra shows bands related to the partial ordering of fluorite structure as reported in literature [21] along with some initial pyrochlore type short range ordering of cation and oxygen vacancies [26-28]. Calcination duration significantly affects

the crystallite size of nanoparticles as it changes from 6nm to 8nm with the change in annealing time from 2h to 6h at 700˚C. XRD patterns of holmium zirconate and holmium hafnate prepared using LAP has been compared and it shows that the difference in the cationic radius of Zr^{4+} and Hf^{4+} in octahedral site affects the XRD peak positions and hence the lattice parameters. Interplanar spacing calculated from XRD and TEM investigations is in excellent agreement with each other as well as with the standard reference data. HR-TEM image of synthesised nanopowder shows the profile view and distinct lattice planes which can be easily indexed to defect fluorite structure of $Ho_2Zr_2O_7$. TEM-EDX analysis confirms that $Ho_2Zr_2O_7$ is stoichiometric. Ion-exchange based Leeds Alginate Process is therefore a highly versatile technique to produce pyrochlore oxide nanoparticles as solid electrolyte materials for solid oxide fuel cells in an environmentally friendly, cost effective and energy efficient manner.

Acknowledgement:

References

[1] L. Yang, Y. Choi, W. Qin, H. Chen, K. Blinn, M. Liu, P. Liu, J. Bai, T. A. Tyson, M. Liu, Promotion of water-mediated carbon removal by nanostructured barium oxide/nickel interfaces in solid oxide fuel cells, Nat Commun. 2 (2011) 357.

[2] C. Zhe, J. H. Wang, Y. M. Choi, L. Yang, M. C.Lin, M. Liu, From Ni-YSZ to sulfur-tolerant anodes: electrochemical behavior, modeling, in situ characterization, and perspectives, Energy Environ Sci Perspect Rev. 4 (2011) 4380–4409.

[3] S. Prabhaker, Q. M. Nguyen, Solid oxide fuel cell technology status, Int. J. Appl. Ceram. Technol. 1:1 (2004) 5-15.

[4] T. A. Vanderah, Talking ceramics, Science. 298 (2002)182-4.

[5] K. Gill, O. P. Pandey, K. Singh, Role of sintering temperature on thermal, electrical and structural properties of $Y_2Ti_2O_7$ pyrochlores, International Journal of Hydrogen Energy. 36 (2005) 14943-7.

[6] M. A. Subramanian, G. Aravamudan, G. V. S. Rao, Oxide pyrochlores-a review, Prog. Solid State Chem. 15 (1983) 55-143.

[7] Shamblin et al., Probing disorder in isometric pyrochlore and related complex oxides, Nature Materials. 15 (2016) 507-12.

[8] W. R. Gombotz, S. F. Wee, Protein release from alginate matrices, Advanced Drug Delivery Reviews. 31:3 (1998) 267-285.

[9] I. D. Hay, Z. U. Rehman. A. Ghafoor, B. H. A. Rehm, Bacterial biosynthesis of alginates, J Chem Technol Biotechnol. 85 (2010) 752–759

[10] Z. Schnepp, S. C. Wimbush, S. Manna, S. R. Hall, Alginate-mediated routes to the selective synthesis of complex metal oxide nanostructures, Cryst. Eng. Comm. 12 (2010) 1410–1415 DOI: 10.1039/b923543b

[11] Z. A. C. Schnepp, S. C. Wimbush, S. Mann, S. R. Hall, Structural Evolution of Superconductor Nanowires in Biopolymer Gels, Adv. Mater. 20 (2008) 1782–1786 DOI:10.1002/adma.200702679,

[12] Z. H. Wang, G. M. Kale, M. Ghadiri, Novel ion-exchange process for the preparation of metal oxide nanopowders from sodium alginate, J. Am. Ceram. Soc. 95 (2012) 3124‑3129 DOI: 10.1111/j.1551-2916.2012.05366.x

[13] Z. Wang, G. M. Kale, M. Ghadiri, Synthesis and characterization of $Ce_xGd_{1-x}O_{2-d}$ nanopowders employing an alginate mediated ion-exchange process, Chem. Eng. J. 198–199 (2012a) 149–153.

[14] Z. Wang, G. M. Kale, Q. Yuanb, M. Ghadiri, X-Ray micro-tomography of freeze dried nickel alginate beads and transformation into NiO nanopowders, RSC Advances. 2 (2012) 9993–9997.

[15] Z. Wang, T. P. Comyn, M. Ghadiri, G. M. Kale, Maltose and Pectin Assisted Sol-Gel Production of $Ce_{0.8}Gd_{0.2}O_{1.9}$ Solid Electrolyte Nanopowders for Solid Oxide Fuel Cells, J. Mater. Chem. 21:41 (2011) 16494‑9.

[16] H. M. Rietveld, A Profile Refinement Method for Nuclear and Magnetic Structures, J. Appl. Crystallogr. 2 (1969) 65‑71.

[17] R. A.Young, The Rietveld Method. Oxford University Press Inc. New York, 1993.

[18] S. Rahayu, J.S. Forrester, G. M. Kale, M. Ghadiri, Promising solid electrolyte material for an IT-SOFC: crystal structure of the cerium gadolinium holmium oxide $Ce_{0.8}Gd_{0.1}Ho_{0.1}O_{1.9}$ between 295 and 1023 K, Acta Cryst. C74 (2018) 236–239.

[19] M. Stopyra, D. Niemiec, G. Moskal, Synthesis, Characterization and Thermal Diffusivity of Holmium and Praseodymium Zirconates, Arch. Metall. Mater. 61:2B (2016) 1249–1254

[20] T. Gladman, Grain Size Control. Maney Publishing, 2004.

[21] F. N.Sayed, D. Jain, B. P, Mandal, C. G. S. Pillai, A. K. Tyagi, Tunability of structure from ordered to disordered and its impact on ionic conductivity behavior in the $Nd_{2-y}Ho_yZr_2O_7$ $(0.0 \leq y \leq 2.0)$ system, RSC Advances. 2 (2012) 8341–8351

[22] S. Sardar, G. M. Kale, M. Ghadiri. Environmentally Sustainable Low Temperature Process for One-step Manufacturing of Nanostructured Holmium Hafnate ($Ho_2Hf_2O_7$). Manuscript for publication, 2018.

[23] R. D. Shannon, Revised effective ionic radii and systematic studies of interatomic distances in halides and chalcogenides, Acta Cryst. A32 (1976) 751–767.

[24] M. Glerup, O.F. Nielsen, F.W. Poulsen, The Structural Transformation from the Pyrochlore Structure, $A_2B_2O_7$, to the Fluorite Structure, AO_2, Studied by Raman Spectroscopy and Defect Chemistry Modeling, J. Solid State Chem.160 (2001) 25–32.

[25] D. L.Rousseau, R. P. Bauman, S. P.S. Porto, Normal mode determination in crystals. J. Raman Spectrosc. 10:1 (1981)253–290.

[26] P. E. R. Blanchard, S. Liu, B. J. Kennedy, C. D. Ling, M. Avdeev, J.B. Aitken, B. C.C. Cowie, A. Tadich, Investigating the local structure of lanthanoid hafnates $Ln_2Hf_2O_7$ via diffraction and spectroscopy, J. Phys. Chem. 115 (2013) 2266–73.

[27] H. C. Gupta, S. Brown, N. Rani, V. B. Gohel, A lattice dynamical investigation of the Raman and the infrared frequencies of the cubic $A_2Hf_2O_7$ pyrochlores, J. Phys. Chem. Solids. 63. (2002) 535–8.

[28] S. Kumar, H. C. Gupta, First principles study of dielectric and vibrational properties of pyrochlore hafnates, Solid State Sci. 14 (2012)1405–11.

[29] F. W. Poulsen, M. Glerup, P. Holtappels, Structure, Raman spectra and defect chemistry modelling of conductive pyrochlore oxides, Solid State Ion. 135 (2000) 595–602.

[30] W. Zhou, F. G. Heather, What can electron microscopy tell us beyond crystal structures? Eur. J. Inorg. Chem. (2016) 941-950.

[31] V. Uvarov, I. Popov, Metrological characterization of X-ray diffraction methods at different acquisition geometries for determination of crystallite size in nano-scale materials, Mater. Charact. 85 (2013) 111–123.

[32] A. N. Chiaramonti, L.D. Marks. "Thickness Series": Weak Signal Extraction of ELNES in EELS Spectra from Surfaces. J. Mater. Res. 20 (2005) 1619–1627.

[33] Gao, et al., Hierarchical assembly of multifunctional oxide-based composite nanostructures for energy and environmental applications, Int. J. Mol. Sci. 13 (2012) 7393–7423.